



Single vector mode transmission in hollow-core photonic bandgap fiber based on surface mode coupling effect

Yong You¹ · Yuanjiang Li¹ · Biao Liu¹ · Yundong Hao² · Yan-Ge Liu²

Received: 3 June 2024 / Accepted: 6 August 2024

© The Author(s), under exclusive licence to Springer Science+Business Media, LLC, part of Springer Nature 2024

Abstract

Relying on the long-distance mode retention capability of hollow core fibers (HCFs) to achieve particle capture and advancement has become a breakthrough in optical tweezers research. This first requires the HCF to get a balance long distance and pure mode. However, the unique light guide mechanism and complex drawing process make it a difficult question to decrease the number of the allowed modes. In this paper, a hollow core photonic bandgap fiber (HC-PBF) that only supports pure TE_{01} mode over 100 nm bandwidth covering the C+L band with the lowest loss of 10.2 dB/km is proposed. The core wall is used as the only control variable to control the coupling position of surface modes (SMs) in the bandgap to filter unwanted modes and achieve stable single-mode transmission in the fiber. The thick core wall allows the fiber to be crimped to a radius of 0.25 mm. Moreover, characteristics such as mode conversion and manufacturing tolerances are also discussed.

Keywords Hollow core photonic bandgap fiber; Surface mode; Mode control; Single-polarization single-mode

1 Introduction

Optical tweezers are a powerful and noninvasive tool for manipulating small objects, and have become indispensable in many fields, including physics, biology, soft condensed matter, among others (Marago et al. 2013; Donato et al. 2018; Arita et al. 2018). In the early days, optical trapping was typically accomplished with a single Gaussian beam. In recent years, we have witnessed rapid progress in the use of cylindrical vector modes in optical trapping. This type of beam has unique transverse and longitudinal force components (also called scattering force and gradient force) in the capture plane. The particles are stably captured in the center of the fiber core through the gradient force to balance the gravity, and then control particle guidance along the fiber axis by scattering forces. When

✉ Yong You
youyongmail@163.com

¹ Ocean College, Jiangsu University of Science and Technology, Zhenjiang 2120033, China

² Tianjin Key Laboratory of Micro-Scale Optical Information Science and Technology, Institute of Modern Optics, Nankai University, Tianjin 300350, China

tightly focused, different polarizations of the input beam can produce different optical forces at the notch plane, which opens a new way for micromanipulation in liquid, air and vacuum. Unfortunately, although considerable effort has been made to enhance the manipulation range of fiber traps, it is limited to a few mm or less by the Rayleigh range or the dimensions of the optical system, even when complex experimental configurations involving spatial light modulators or nondiffracting Bessel beams are used (Čižmár et al. 2005). HCF allows optical trapping and propulsion of individual microparticles within the fiber core over distances limited only by the fiber loss (Sharma et al. 2021), making them useful in applications such as optical conveyor belts (Schmidt et al. 2013), flying particle sensing (Bykov et al. 2015; Sharma et al. 2019), and on-the-fly particle metrology (Bykov et al. 2018). Compared to free-space geometries, HC-PBF optical tweezers can break the control range to the meter level, and protect particles from airflow, forming a unique long-manipulation research platform (Xie et al. 2021; Wang et al. 2024).

Due to the multimode operation of HC-PBF, multimode scattering occurs when the light beam encounters suspended particles, resulting in a multimode beat pattern along the fiber axis. Multimode group velocity walk-off can eliminate unnecessary multimode jumps in the fiber (Sharma et al. 2021), but if flexible single-mode guidance can be directly implemented in the fiber, the system complexity will be greatly simplified. HC-PBFs integrates the advantages of spatial stability, reduced optical nonlinearity, environmental insensitivity and bending flexibility, allowing light waves to travel at near-physical limits in air core with minimal field-material interaction domains (Poletti et al. 2013; Fokoua et al. 2017; You et al. 2021a; Yang et al. 2020a). Since air can't withstand anisotropy, the solution for single mode operation in traditional solid core fibers is not applicable for HC-PBF. Although some special microstructures are reintroduced to achieve excellent polarization effect (Watari et al. 2020; You et al. 2021b; Zhu et al. 2021), but the actual fiber drawing process limited the operational space for mode control (Yang et al. 2020b). An efficient method is achieved by introducing the shunt core to provide the purity of the mode and glass node placed asymmetrically at the core boundary to impose a large birefringence, paid the price of reduced bandwidth (~ 10 nm) due to SM limitation (Fini et al. 2014).

SMs are important modes in HC-PBF, which are physically confined to the core-surrounding interface and are spectrally guided at wavelengths within the bandgap (Lamilla et al. 2018). These modes may lead to strong attenuation of the transmission spectrum and reduction of the available bandwidth. Many efforts have been devoted to eliminating the coupling effect of SMs on core mode (CM) (Micheletto et al. 2014; Zhang et al. 2019). However, for well-designed fiber structures, high birefringence and low loss can be achieved through the anti-cross coupling of SMs (Yu et al. 2024), and they can also be used as control tools to achieve mode number or temperature dependent group delay (You et al. 2021c; Wang et al. 2022). According to relevant research, the wall thickness between the core and cladding has a significant impact on the mode characteristics of HC-PBF (Tian et al. 2024). As the wall thickness increases, SM only couples with a unique core mode, resulting in high loss characteristics of the core mode within a certain bandwidth range (You et al. 2021c). These findings inspired us to use the coupling rules of SMs for mode control.

In this paper, the SM coupling rules in HC-PBF are fully utilized to achieve flexible mode control. The core wall thickness is the only control variable to achieve complete filtering of all CMs with a bandwidth exceeding 100 nm except TE_{01} , which greatly simplifies the stringent requirements for fiber drawing process. The designed fiber has a lowest loss of 10.2 dB/km, and the loss is less than 19 dB/km in the range of

1515–1605 nm, while other CMs are greater than 100 dB/km. $\Delta n_{eff} > 1.0 \times 10^{-3}$ makes TE_{01} completely unaffected by any mode coupling in the entire single-mode window. The tunability of the single-mode window can be achieved by adjusting the wall thickness. The thicker core wall ensures excellent bending insensitivity, and bending losses only increase significantly when the bending radius is less than 0.25 mm. Furthermore, the principle of SMs coupling for single mode conduction is analyzed, and the coupling characteristics of each SMs are summarized separately. Mode conversion and manufacturing tolerances are also discussed.

1.1 Fiber structure and performance

The structure of HC-PBF is more complex compared to hollow core anti-resonant fiber (HC-ARF) and requires higher drawing processes to achieve precise structural control. Therefore, to avoid adding additional structures, the fiber model should maintain the original stacked shape of glass tubes as much as possible. As shown in Fig. 1, it is the cross-sectional structure and key parameters of the designed fiber. The structure parameters are set to typical values to meet the minimum loss and maximum bandwidth of the mode near 1550 nm wavelength. The lattice constant $\Lambda = 4 \mu\text{m}$, the cladding air hole diameter $d = 0.98\Lambda$, the wall thickness around the core t is specially set to 232 nm to achieve single mode transmission based on SM coupling. The core defect made by removing 7-unit cells resembles a dodecagon with a radius of $R = 6 \mu\text{m}$. Besides, the fillet diameters of the cladding and core are: $d_c = 0.3\Lambda$, $d_t = 0.6\Lambda$. The full-vector finite element method is used to calculate mode characteristics. The background material is pure silica, and the refractive index at different wavelength is determined by the Sellmeier equation. The material dispersion is neglected since the light propagates mainly in the air.

Generally, the simulated results of the fiber characteristics can't replace the test results of actual fibers, because precise design requirements and inherent sensitivity of HCF geometries pose great challenges to the drawing process, which prohibits the conversion of excellent designs into products in many cases. However, the thickness of the core wall

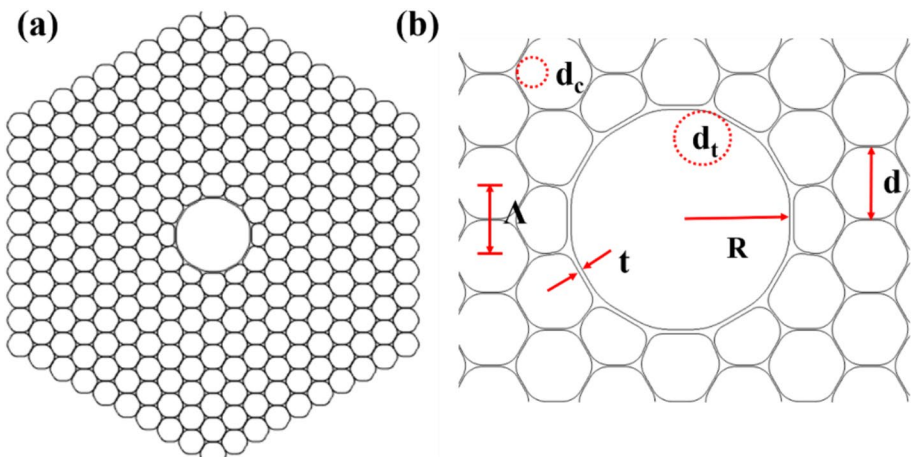


Fig. 1 Cross-section structural parameters and schematic diagram of realizing single TE_{01} mode transmission

here is the only control variable for single mode transmission, which greatly reduces the requirements for the fiber drawing process. In this part, the single-mode window formation mechanism based on the SM coupling rule is explained in detail. Normalized core wall thickness is defined to more refined characterize the coupling rule of SMs.

$$T = \frac{t}{\Lambda - d}, \quad (1)$$

where $\Lambda - d$ represents the wall thickness of the cladding air holes, and the larger T is, the thicker the core wall is.

The loss of the 7-cell HC-PBF is the sum of scattering and confinement loss, where the scattering loss is obtained by the empirical formula (Wang et al. 2022):

$$SSL[dB/km] = \eta F \left(\frac{\lambda[\mu m]}{\lambda_0} \right)^{-3} \quad (2)$$

where F is the optical power overlap between the core mode and the silica core boundary, and $\eta = 300$, representing the calibration factor at a wavelength of $\lambda_0 = 1.55 \mu m$.

The confinement loss is obtained from the imaginary part of the effective mode refractive index (Wang et al. 2022):

$$CL[dB/km] = \frac{40\pi Im(n_{eff})}{Im(10)\lambda[m]} 10^3, \quad (3)$$

where $Im(n_{eff})$ is the imaginary part of the mode effective refractive index.

Many simulations show that the SMs in HC-PBF follow a certain changes rule. The core wall thickness can control the movement of all SMs within the bandgap at a fixed speed. When the core wall thickness is thin, such as in the $T/2$ condition (i.e., the core wall thickness is half of the cladding wall thickness), all SMs will be suppressed outside the short wavelength bandgap. As the wall thickness increases gradually, SMs will enter the bandgap in turn. They will only couple with the unique corresponding CM and will not interfere with other CMs. Different SMs have different coupling bandwidths and have different effects on the CMs. Therefore, the mode control in HC-PBF can be achieved through unified control of SMs.

The premise of mode control requires us to have a full understanding of the coupling characteristics of these SMs. The HC-PBF model in Fig. 1 is used as an observation platform for the coupling process of SMs. We gradually increase T from 0.5 to 4, and analyze characteristics of SMs coupled with HE_{11} , TE_{01} , HE_{21} and TM_{01} in turn. The detailed summary characteristics are shown in Table 1. When $T=0.8$, the first SM coupled with HE_{11} appears, which we call SM1- HE_{11} . It will move to the long-wavelength direction with the increase of T at a speed of 46 nm/0.1 T . When $T=1.6$, SM1- HE_{11} disappears from the bandgap edge. After that, SM2,3 and so on will appear in the bandgap in turn and move at different coupling speeds. In the range of $T=0.5-4$, a total of 9 SMs appear in the bandgap, with the maximum coupling bandwidth exceeding 120 nm, and the minimum only 20 nm. The first SM coupled with TE_{01} is named SM1- TE_{01} . When $T=0.6$, SM1- TE_{01} appears in the bandgap. When $T=4$, there are a total of 4 different SMs coupled with TE_{01} , with the

Table 1 Summary of SMs coupling characteristics of HE_{11} , TE_{01} , HE_{21} and TM_{01} in 7-cell HC-PBF

	HE_{11}	TE_{01}	HE_{21}	TM_{01}
Number of SMs	9	4	10	3
Maximum coupling bandwidth	80 nm	140 nm	100 nm	120 nm
Minimum coupling bandwidth	3 nm	2 nm	3 nm	10 nm

maximum coupling bandwidth exceeding 140 nm and the minimum 2 nm. When $T=0.8$, SM1-HE₂₁ begins to appear in the bandgap. When $T=4$, a total of 7 SMs are coupled to HE₂₁, the largest of which exceeds 100 nm, and the smallest is only 3 nm. SM1-TM₀₁ appears in the bandgap when $T=1.6$, and only 3 SMs are coupled with TM₀₁ when $T=4$. The maximum coupling bandwidth is 120 nm, and the minimum is 10 nm. Although there are few SMs, each SM has a wide coupling bandwidth with TM₀₁ due to its out-of-plane polarization direction.

Here, we analyze the evolution rules of SMs coupled with CMs when $T=2.9$ (i.e., $t=232$ nm), because when T is set to this value, all modes except TE₀₁ can be fully coupled by SMs, thereby maintaining the maximum single-mode window. The CMs are analyzed independently, and the coupling effects of SMs on the loss spectrum can be visually seen. As shown in Fig. 2, the mode fields, coupling bandwidths and coupling speeds of SMs in the single mode window are studied in detail. Figure 2a shows the loss spectra of HE₁₁, TM₀₁ and HE₂₁. The shaded part represents the bandwidth area where the CM loss due to SMs coupling is greater than 10 dB/km. Figure 2b shows the mode field coupling diagrams of SMs and CMs in the coupling wavelength. Figure 2c shows the movement rules of the center wavelength of SM and CM coupling in the bandgap with the increases of T , according to which the mode control can be flexibly selected in the desired wavelength range. Among them, HE₁₁ is co-coupled by SM4-HE₁₁ and SM5-HE₁₁ to form a 160 nm high loss region. With the increase of T , SM4-HE₁₁ and SM5-HE₁₁ move toward the long

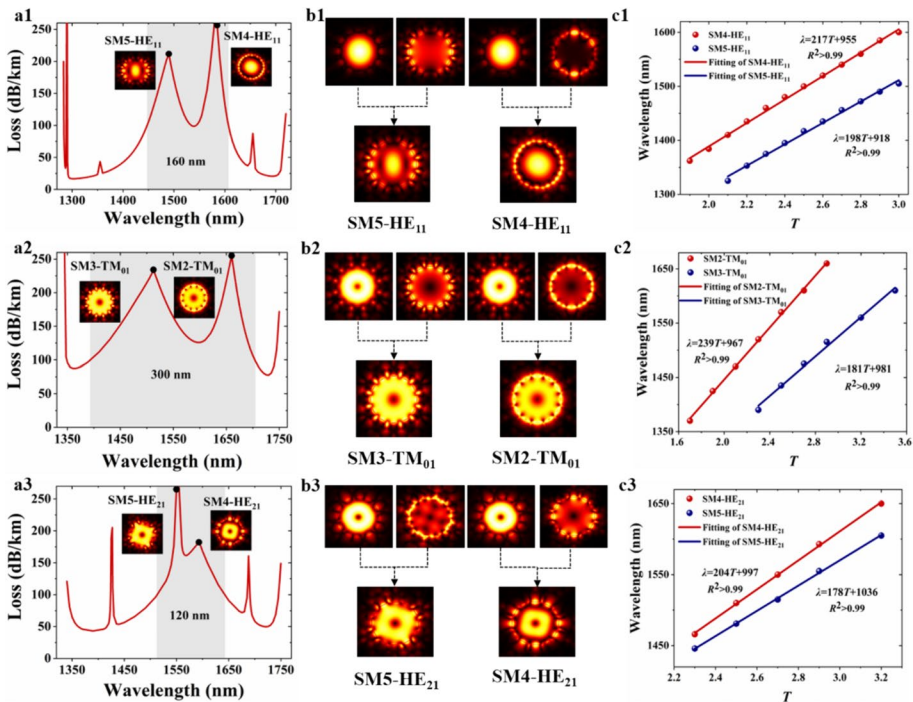


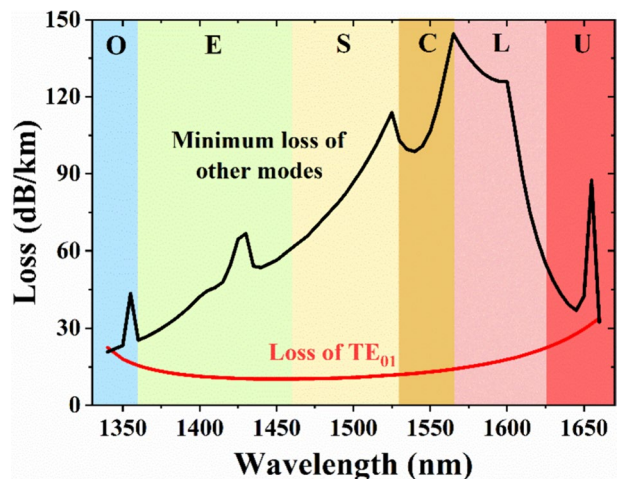
Fig. 2 SMs coupling rules for HE₁₁, TM₀₁ and HE₂₁ in the single mode window when $T=2.9$ (i.e., $t=262$ nm): **a** loss spectra and coupling bandwidths, **b** diagrams of SMs and CMs coupling process, **c** moving rate of SMs as T increases

wavelength at 21.7 nm/0.1 T and 19.8 nm/0.1 T , respectively. TM_{01} is co-coupled by $SM2-TM_{01}$ and $SM3-TM_{01}$ to form a 300 nm high loss region. $SM3-TM_{01}$ and $SM2-TM_{01}$ move toward the long wavelength at 18.1 nm/0.1 T and 23.9 nm/0.1 T , respectively. HE_{21} is co-coupled by $SM4-HE_{21}$ and $SM5-HE_{21}$ to form a high loss region of 120 nm. $SM4-HE_{21}$ and $SM5-HE_{21}$ move toward the long wavelength at the speeds of 20.4 nm/0.1 T and 17.8 nm/0.1 T , respectively. By comparison, it can be found that the high loss bandwidth of TM_{01} is much larger than that of HE_{11} and HE_{21} . TE_{01} is not affected by SMs at this wall thickness, and it always maintains low-loss transmission in the bandgap.

The loss contrast of the designed fiber in the single-mode window formed by TE_{01} and other CMs with minimal loss is shown in Fig. 3. The red curve is the loss spectrum of TE_{01} in the bandgap. The loss is less than 20 dB/km in the range of 1350–1620 nm, and the minimum loss is 10.2 dB/km at 1450 nm. The black curve is the loss spectrum drawn by other CMs (HE_{11} , HE_{21} , TM_{01}) with minimal loss. Several spikes in the loss spectrum indicate the coupling centers of the SMs. The coupling effects of SMs in the CMs are different, some can cause CM to form a high loss bandwidth exceeding 100 nm, while some have only a few nm. Therefore, the gradually rising black loss spectrum indicates that the close to the coupling center of the SMs with wide coupling bandwidths, where the loss is greater than 100 dB/km in the range of 1515–1605 nm, which covers entire C-band and part of the S and L-band ranges. In the C+L band, all CMs except TE_{01} are suppressed by their respective SM coupling, and the corresponding losses are: $TE_{01} \sim 13$ dB/km, $HE_{11} \sim 107$ dB/km, $TM_{01} \sim 163$ dB/km, $HE_{21} \sim 265$ dB/km at 1550 nm.

It is generally believed that the mode coupling of HCF is much weaker than that of SCF, because the extremely low interaction of optical modes with the fiber cladding. Figure 4 shows the main characteristics of the designed fiber to clarify the single-mode transmission effect. Due to the deliberately selected core wall thickness, TE_{01} can be guaranteed to be completely free from coupling interference from other modes. Figure 4a draws the effective refractive index curves of the fundamental mode and the 1st vector modes, where the red curve represents TE_{01} . TE_{01} is always continuous and smooth within the bandgap and is not affected by SMs. Other CMs are coupled by SMs to different degrees, which results in large distortion of the curves and causes the close curves of CMs to be completely separated, which avoids the coupling interference of other CMs to TE_{01} . In Fig. 4b, the Δn_{eff}

Fig. 3 Loss contrast between TE_{01} and other modes with minimal loss in the designed fiber (confinement loss + scattering loss)



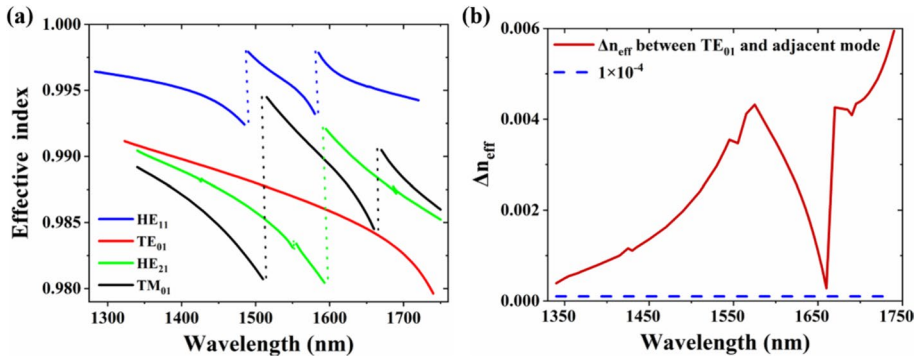


Fig. 4 The main characteristics of the CMs in the bandgap: **a** effective refractive index, **b** loss

between TE₀₁ and the nearest CMs is plotted, and it is obvious that there is a sufficiently large interval between them: TE₀₁ ~ Δn_{eff} > 10⁻³. Therefore, within the wavelength range of more than 100 nm, the transmission of TE₀₁ will not be disturbed by other adjacent modes.

1.2 Bending stability

Bending loss of fibers is a key feature when faced with application requirements in complex and narrow environments. We have evaluated the effect of bending on fiber performance. Here, an equivalent method is used to simulate the proposed fiber for bend condition, which modifies the n_{eff} of an equivalent straight fiber to emulate the bending effect (Poletti 2014).

$$n_i' = n_i \cdot e^{\left(\frac{x}{R_c}\right)} \approx n_i \cdot \left(1 + \frac{x}{R_c}\right), \quad (4)$$

Where R_c is the radius of curvature, x is the distance from the center of the waveguide, n_i is the original refractive index distribution of the straight fiber.

The simulated dependence of the bending loss of TE₀₁ in the x bending directions with different radius values is shown in Fig. 5a (at 1550 nm). Obviously, bending insensitivity of the designed HC-PBF is further enhanced due to the thicker core wall. It can even be coiled to a small bend radius of 0.25 mm. Fig. 5b shows the mode field energy distribution of TM₀₁, HE₂₁ and HE₁₁ under bending conditions. Due to the coupling effect with SMs, the energy of CMs is more easily lost to the SMs even under weak bending strength. Therefore, the designed fiber can ensure better single-mode bending resistance in narrow bending environments.

2 Discussion

The proposed method realized precise mode control without introducing additional changes in the fiber structure, greatly simplifying the difficulty of fiber drawing. Due to the experimental conditions, we can't pull the designed fiber into a finished product. But at the beginning of the design, our goal was to keep the structure as close to existing fiber products as possible. The key structural parameters in the model, are close to the current

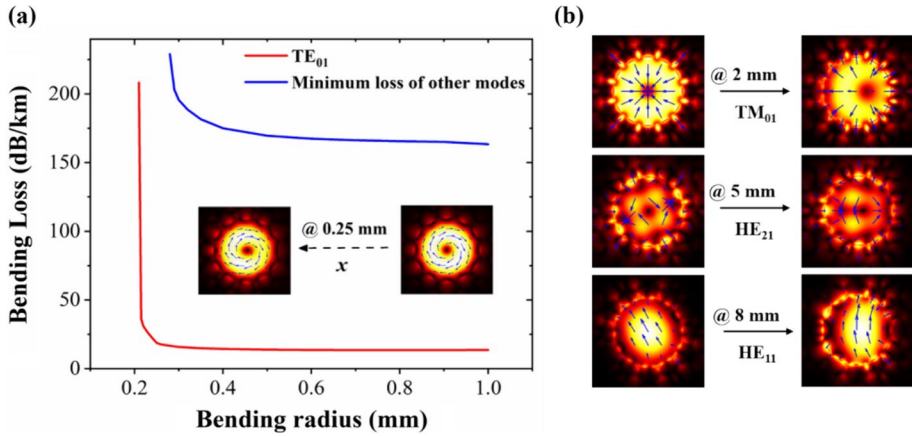


Fig. 5 Bending characteristics of designed fiber at 1550 nm. **a** Simulated dependence of the bending loss of TE_{01} in the x bending directions with different radii. The insets show the mode field changes. **b** the mode field distribution and bending sensitivity radii of other CMs

mature product NKT 1550-02 (https://www.newport.com.cn/medias/sys_master/images/images/he1/hc5/8797092347934/FAIR-11-1550-Data-Sheet.pdf). To provide a reference for the actual fabricated, here we quantitatively analyze the impact of the key structural parameters on the single-mode filtering effect. In Fig. 6a, the loss comparison between TE_{01} and other modes with minimum loss under different normalization core wall thickness is shown, the gray area is the manufacturing tolerance. In the range of 2.8–3.0 (t : 224–240 nm), the loss of TE_{01} is always less than 15 dB/km, while other modes is greater than 120 dB/km, and the single-mode filtering effect is well maintained, which provides us with a high manufacturing tolerance. Meanwhile, the loss comparison between TE_{01} and other modes under different lattice diameters is also discussed, as according to formula (1), d will have an import on T . As illustrated in Fig. 6b, in the range of 0.979–0.981 Λ , the loss of TE_{01} is less than 16.75 dB/km, whereas the losses for other modes exceed 100 dB/km, maintaining a relatively good single-mode performance. Among them, the blue marks in the figure are the ideal structure parameters of the proposed fiber.

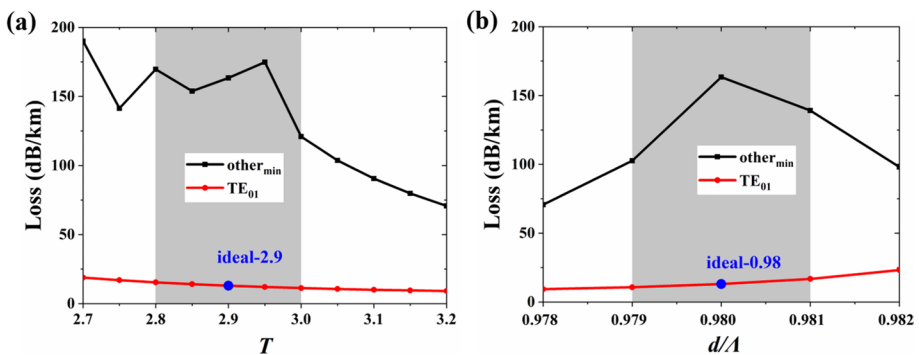


Fig. 6 Manufacturing tolerance of key parameters: **a** loss comparison of different normalization core wall thickness, **b** cladding lattice diameters. The blue marks are the ideal parameters of the proposed fiber

The proposed single-mode single-polarization HC-PBF is based on SMs coupling to realize the transmission of TE_{01} instead of the fundamental mode or other CMs. This is because TE_{01} has the lowest transmission loss in HC-PBF (Kubota et al. 2018). On the other hand, the near-circular fiber core in the model makes TE_{01} less affected by SM coupling, while other CMs are more affected by SM. Therefore, retaining TE_{01} can achieve lower loss and wider bandwidth single-mode transmission. Of course, for the individual transmission of other CM, the fiber structure can be optimized according to the mode field characteristics of the corresponding CM, and then the regulation can be realized according to the summarized SMs coupling rules. It is also possible to convert TE_{01} to other CMs at the fiber output end through a more efficient mode converter, such as TM_{01} , which has richer application requirements.

3 Conclusion

In this paper, we proposed an effective method to realize single-mode single-polarization transmission by using SMs coupling in HC-PBF. The precise control of SM coupling rule is achieved by adjusting the unique control variable core wall thickness. We found that each CM has coupled SMs, which do not couple with other CMs. They enter the bandgap at different coupling bandwidths and coupling speeds, and they all have a linear relationship with the core wall thickness. According to the coupling rules, efficient mode control can be achieved by setting the wall thickness within an appropriate range. The simulation results show that pure TE_{01} transmission over 100 nm can be achieved when $T=2.9$, and the remaining CMs are resonantly coupled by SMs. The loss of TE_{01} is less than 19 dB/km in the range of 1515–1605 nm, while other CMs are all great than 100 dB/km. And TE_{01} also has a large enough Δn_{eff} to avoid any mode coupling effects. In addition, the fiber has excellent bending stability with a bending radius of 0.25 mm. The proposed fiber could be a potential candidate for particle manipulation because of its hollow-core structure, single-polarization single-mode guidance, and high stability performance.

Author contribution Yong You wrote the main manuscript text and prepared all figures. Biao Liu and Yundong Hao checked the paper and provided revision suggestions. All authors reviewed the manuscript.

Funding National Natural Science Foundation of China, No.62276117; Jiangsu Provincial Natural Science Foundation General Project, BK20231257.

Data availability No datasets were generated or analysed during the current study.

Declarations

Conflict of interest The authors declare no conflicts of interest

References

- Arita, Y., Wright, E.M., Dholakia, K.: Optical binding of two cooled micro-gyroscopes levitated in vacuum. *Optica* **5**(8), 910–917 (2018)
- Bykov, D.S., Schmidt, O.A., Euser, T.G., Russell, P.S.J.: Flying particle sensors in hollow-core photonic crystal fibre. *Nat. Photonics* **9**(7), 461–465 (2015)

- Bykov, D.S., Xie, S., Zeltner, R., Machnev, A., Wong, G.K.L., Euser, T.G., Russell, P.S.J.: Long-range optical trapping and binding of microparticles in hollow-core photonic crystal fibre. *Light. Sci. Appl.* **7**(1), 1–7 (2018)
- Čižmár, T., Garcés-Chávez, V., Dholakia, K., Zemánek, P.: Optical conveyor belt for delivery of submicron objects. *Appl. Phys. Lett.* **86**(17), 1741011–1741013 (2005)
- Donato, M.G., Brzobohaty, O., Simpson, S.H., Irrera, A., Leonardi, A.A., Lo Faro, M.J., Svak, V., Marago, O.M., Zemánek, P.: Optical trapping, optical binding, and rotational dynamics of silicon nanowires in counter-propagating beams. *Nano Lett.* **19**(1), 342–352 (2018)
- Fini, J.M., Nicholson, J.W., Mangan, B., Meng, L., Windeler, R.S., Monberg, E.M., DeSantolo, A., DiMarcello, F.V., Mukasa, K.: Polarization maintaining single-mode low-loss hollow-core fibres. *Nat. Commun.* **5**(1), 5085–5087 (2014)
- Fokoua, E.N., Petrovich, M.N., Bradley, T., Poletti, F., Richardson, D.J., Slavik, R.: How to make the propagation time through an optical fiber fully insensitive to temperature variations. *Optica*. **4**(6), 659–668 (2017)
- https://www.newport.com.cn/medias/sys_master/images/images/he1/hc5/8797092347934/FAIR-11-1550-Data-Sheet.pdf
- Kubota, H., Kosake, N., Miyoshi, Y., Ohashi, M.: Unique loss characteristics in TE₀₁ modes of conventional photonic bandgap fibers. *Opt. Lett.* **43**(11), 2599–2602 (2018)
- Lamilla, E., Faria, M.S., Aldaya, I., Jarschel, P.F., Pita, J.L., Dainese, P.: Characterization of surface-states in a hollow core photonic crystal fiber. *Opt. Expr.* **26**(25), 32554–32564 (2018)
- Marago, O.M., Jones, P.H., Gucciardi, P.G., Volpe, G., Ferrari, A.C.: Optical trapping and manipulation of nanostructures. *Nat. Nanotech.* **8**(11), 807–819 (2013)
- Michieletto, M., Lyngsø, J.K., Laegsgaard, J., Bang, O.: Cladding defects in hollow core fibers for surface mode suppression and improved birefringence. *Opt. Expr.* **22**(19), 23324–23332 (2014)
- Poletti, F.: Nested antiresonant nodeless hollow core fiber. *Opt. Expr.* **22**(20), 23807–23828 (2014)
- Poletti, F., Petrovich, M.N., Richardson, D.J.: Hollow-core photonic bandgap fibers: technology and applications. *Nanophotonics*. **2**(6), 315–340 (2013)
- Schmidt, O.A., Euser, T.G., Russell, P.S.J.: Mode-based microparticle conveyor belt in air-filled hollow-core photonic crystal fiber. *Opt. Expr.* **21**(24), 29383–29391 (2013)
- Sharma, A., Xie, S., Zeltner, P., Russell, P.S.J.: On-the-fly particle metrology in hollow-core photonic crystal fiber. *Opt. Expr.* **27**(24), 34496–34504 (2019)
- Sharma, A., Xie, S., Russell, P.S.: Reconfigurable millimeter-range optical binding of dielectric microparticles in hollow-core photonic crystal fiber. *Opt. Lett.* **46**(16), 3909–3912 (2021)
- Tian, X., Lou, S., Gao, W., Jia, H., Lian, Z., Wang, X.: Effects of selectively thickening core wall on birefringence and loss in polarization-maintaining hollow core photonic bandgap fiber. *Opt. Quant. Electron.* **56**(5), 856 (2024)
- Wang, Y., Li, Z., Yu, F., Wang, M., Han, Y., Hu, L., Knight, J.: Temperature-dependent group delay of photonic-bandgap hollow-core fiber tuned by surface-mode coupling. *Opt. Expr.* **30**(1), 222–231 (2022)
- Wang, R., Li, K., Liu, X., Jiang, Y., Yin, R., Zheng, Y., Jiang, X., Xie, S.: Non-markovian doppler velocimetry of optically propelled microparticles in hollow-core photonic crystal fiber. *ACS Photonics* **11**(4), 1533–1539 (2024)
- Watari, N., Takano, A., Naito, A., Watanabe, T., Fujiya, Y., Ishide, T.: Fractal photonic bandgap fibers. *Opt. Expr.* **28**(22), 33184–33197 (2020)
- Xie, S., Sharma, A., Romodina, M., et al.: Tumbling and anomalous alignment of optically levitated anisotropic microparticles in chiral hollow-core photonic crystal fiber. *Sci. Adv.* **7**(28), 6053–6062 (2021)
- Yang, F., Gyger, F., Thévenaz, L.: Intense Brillouin amplification in gas using hollow-core waveguides. *Nat. Photonics* **14**(11), 700–708 (2020a)
- Yang, Y., Homma, O., Urata, S., Ono, M., Mauro, J.C.: Topological pruning enables ultra-low rayleigh scattering in pressure-quenched silica glass. *Npj. Comput. Mater.* **6**(1), 1–8 (2020b). <https://doi.org/10.1038/s41524-020-00408-1>
- You, Y., Guo, H.Y., Feng, M., Mao, B.W., Shi, H.M., Du, J.B., Wang, Z., Liu, Y.G.: High-order mode characteristics of a 7-cell hollow-core photonic bandgap fiber. *J. Lightwave Technol.* **39**(13), 4469–4477 (2021a)
- You, Y., Guo, H.Y., Hao, Y.D., Wang, Z., Liu, Y.G.: Wideband, large mode field and single vector mode transmission in a 37-cell hollow-core photonic bandgap fiber. *Opt. Expr.* **29**(15), 24226–24236 (2021b)
- You, Y., Liu, Y.G., Hao, Y.D., Guo, H.Y., Wang, Z.: Accurate control of surface modes in a hollow-core photonic bandgap fiber. *IEEE Photonics J.* **14**(1), 1–6 (2021c)

- Yu, F., Chao, S., Wu, D., Chen, S.: Surface-mode induced high birefringence in a low-loss 7-cell photonic bandgap hollow-core fiber. *Optics Express*. (2024)
- Zhang, X., Gao, S., Wang, Y., Ding, W., Wang, X., Wang, P.: 7-cell hollow-core photonic bandgap fiber with broad spectral bandwidth and low loss. *Opt. Expr.* **27**(8), 11608–11616 (2019)
- Zhu, Y., Song, N., Gao, F., Xu, X.: Single-polarization single-mode hollow-core photonic-bandgap fiber with thin slab waveguide. *Opt. Expr.* **29**(19), 30371–30383 (2021)

Publisher's Note Springer Nature remains neutral with regard to jurisdictional claims in published maps and institutional affiliations.

Springer Nature or its licensor (e.g. a society or other partner) holds exclusive rights to this article under a publishing agreement with the author(s) or other rightsholder(s); author self-archiving of the accepted manuscript version of this article is solely governed by the terms of such publishing agreement and applicable law.